Optimizing Top-Mounted Anemometer Boom Height for Micro UAV Wind Measurement

Kate Melody Wiliem[*1], Gihyun Kim[2], Chi-Ying Chan[3], Chun Ho Liu[4], and Adriana Cecilia Zurita Pimentel[5]

[1,2,3,4] *Department of Mechanical Engineering, The University of Hong Kong*

12 September 2026

Abstract

Capturing accurate wind data in densely populated cities like Hong Kong is vital for predicting extreme weather, tracking toxic air pollution, and combating rising urban temperatures. Traditional weather towers are often too bulky, inflexible, and expensive to deploy in these cramped urban spaces. Small drones, or micro-UAVs, offer a highly mobile alternative, compared to professional drones which require a license to fly, but they introduce a new problem: their spinning propellers generate chaotic, turbulent air that severely distorts the readings of onboard wind sensors. This study investigated the optimal mounting height for a Trisonica mini ultrasonic anemometer on a DJI Mavic 3E micro-UAV to bypass this propeller interference. By testing sensor boom lengths ranging from 5 cm to 20 cm, we discovered that a 20 cm boom yields the highest measurement accuracy and the lowest flow disturbance. Interestingly, testing at 10 cm revealed a localized aerodynamic "quiet zone," offering a compact, stable alternative that still achieves over 70% of the error reduction seen at the maximum height.

1 Nomenclature

- **Root Mean Square Error (RMSE):** A statistical measurement of how far off the drone's wind sensor readings are compared to the actual, undisturbed background wind. The higher the RMSE, the greater the aerodynamic interference. As you increase the boom distance away from the propeller, RMSE drops significantly because the sensor escapes the chaotic rotor wash and approaches true ambient conditions.

- **Mean v_i (Induced Velocity):** The average extra speed of airflow generated specifically by the spinning propellers. This directly tracks the strength of the propeller's suction. When the sensor is close to the drone body, mean v_i is very high; as the boom extends further out, mean v_i decreases toward zero as the sensor moves out of the direct downwash path.

- **Composite Ambient Baseline:** The overall average speed of natural background wind measured away from the drone's interference, serving as the benchmark for truth. It acts as the anchor reference for all error calculations. If background weather conditions change and the baseline speed shifts, it alters the relative disruption scale, making it necessary to use normalized metrics for fair comparisons across different days.

- **Reading Scatter / Standard Deviation:** A measure of how wildly air speeds fluctuate over time due to turbulent, chaotic air pockets. Higher scatter indicates a more unstable airflow. Close to the propeller, turbulent eddies cause huge swings in standard deviation; farther out on an optimized boom, the scatter smooths out to reflect the steadier profile of natural wind.

- **Exceedance Rate (%):** The percentage frequency at which wind disturbances cross a specific error limit, such as greater than 1.0 m/s. It defines the threshold of diminishing returns. It pinpoints the exact distance where extending the boom further stops providing meaningful improvements in data quality, helping you balance sensor accuracy against structural limits.

- **Boom Length and Stability (The Lever Effect):** The physical distance the wind sensor is mounted away from the drone. Longer booms improve wind data but harm mechanical stability. While extending the boom moves the sensor

*Corresponding email: katemelody@gmail.com

out of rotor wash, long booms exceeding 20 cm act as heavy levers that introduce structural vibrations, throw off the drone's center of gravity, and strain the flight controller.

- **Inflow Tilt Angle:** An angle measuring the direction air is being pulled into the blades. The closer the inflow tilt angle is to 0 degrees, the weaker the propeller's interference. A steep negative angle means the sensor is trapped inside a powerful downward suction cone; as it approaches 0 degrees, it proves the sensor has moved far enough away to measure pure horizontal outdoor wind.

- **Disturbance Ratio ($v_i/V_{ambient}$):** A normalized metric comparing induced wind velocity against background weather conditions. It neutralizes day-to-day weather variations. Because outdoor wind changes constantly, raw speeds can mislead you; the disturbance ratio tells you how many times stronger the rotor suction is relative to the current real wind, ensuring consistent comparisons across different test flights.

- **Anemometer:** A highly sensitive instrument mounted on the drone used to measure the exact speed and direction of the wind. Its placement dictates data fidelity. If mounted too close to the drone, its readings are completely dominated by rotor wash rather than environmental wind, making correct boom positioning vital to its performance.

- **Rotor Wash (Propeller-Induced Flow):** The turbulent, messy jet of downward air created when drone propellers spin to generate lift. Its intensity scales directly with thrust and proximity. The closer the sensor is to the spinning blades, the stronger the suction zone and chaos it experiences; the strength of this wash drops off exponentially with distance.

- **Stagnation Point:** A specific spot near the top of the drone's body where air movement stops completely, creating a slight upward pressure. It acts as a natural buffer against downwash. This localized upward pressure zone can subtly help cancel out some of the downward suction created by the propellers, altering local airflow depending on how wind wraps around the drone's chassis.

- **Disk Loading:** A mathematical ratio comparing the total weight of the drone to the total circular area its spinning propeller blades cover. Disk loading increases when a drone gets heavier or uses smaller blades. Because more weight is packed into a smaller blade area, the propellers must work much harder, scaling up the intensity of the rotor wash and requiring a longer boom to escape the larger disturbance zone.

- **Multirotor:** An aircraft propelled and lifted by multiple vertical rotors (e.g., quadcopters, hexacopters). Because multiple rotors spin simultaneously, their individual wake fields overlap and interact heavily, creating a complex, turbulent interference zone beneath and around the frame that requires longer boom configurations to bypass cleanly.

- **Fixed Wing:** An aircraft that generates lift through the forward motion of stationary wings rather than spinning overhead blades. Unlike multirotors, fixed-wing platforms experience clean, freestream airflow over their wings during forward flight, avoiding the continuous, localized downwash and propeller suction that complicates onboard wind sensing.

- **Single Rotor:** A helicopter-style configuration utilizing one large main lifting rotor and a tail rotor to counteract torque. Generates a massive, concentrated column of downward slipstream directly beneath the main rotor disk, creating a powerful asymmetrical rotor wash zone that severely impacts sensor placement compared to distributed multirotor setups.

2 Introduction

Wind data collection is essential to everyday life: from prediction of natural disasters (forest fires, cyclones, coastal hazards, etc.); to observing the atmospheric boundary layer, allowing accurate weather forecasts, study of air pollution, optimizing of wind energy; urban planning and agriculture; to studying greenhouse gases and climate change. Moreover, wind data is crucial for calculations to design solutions for precision farming and smart agriculture, solar energy generation, urban heat island effect, and HVAC (Heating, Ventilation and Air Conditioning) systems [1, 2]. In Hong Kong, these uses are even more important.

Firstly, the city is the world's most active cyclone basin [3], experiencing 5-6 tropical cyclones per year on average [4]. Super Typhoon Mangkhut (2018) caused more than 60,000 fallen trees, injured 458+ people, caused power outages for 13 500 households lasting more than 24 hours [5], and resulted in HK

$4.6 billion in direct economic losses [6]. Consequently, accurate wind information becomes critical to predict typhoon levels, timing and scope.

Secondly, due to being one of the most densely populated cities in the world, Hong Kong's high building mass and low ventilation causes it to experience severe urban island heat effect (UHI) [7]. During the day, the city's large areas of glass, asphalt, and concrete absorb solar radiation, then slowly leak the trapped heat back into the air long after the sun goes down, causing urban districts to experience winter temperatures 7.0-8.0°C higher than rural areas [8]. As a result, the annual number of "Hot Nights" ($T \geq 28$°C) in Hong Kong has increased from 2.2 days/yr in 1914 to 52 days in 2022 [9], impacting the comfort and health of its 7.5 million residents. As temperatures rise, air conditioning usage surges, resulting in further global warming [10].

Finally, air pollution represents a critical public health and economic crisis in Hong Kong, where there are 373 licensed vehicles per kilometer of road [11], among the highest globally (compared to 42 in the US) [12, 13]. This is because tall skyscrapers lining both sides of the road block ambient breezes, creating a "street canyon" and stagnating air (0.3-0.8 m/s). This stagnancy prevents pollution dispersion: it traps toxic fumes from vehicle emissions at ground level where pedestrians walk and breathe. [14]. Annually, this results in roadside nitrogen dioxide (NO_2) and fine particulate matter ($PM_{2.5}$) concentrations to 550% and 300% above World Health Organization guidelines, respectively, leading to over 3,500 premature deaths and HK$42 billion in economic losses [15].

Extensive wind data collection is needed to address these problems. However, traditional measurement methods such as meteorological towers, weather stations and weather balloons are less portable, require space, high initial cost, long planning and construction time, and continuous maintenance [1, 16]. In Hong Kong, severe space scarcity renders these methods even more impractical, a 2030+ Hong Kong study predicting a 1200+ ha land shortage in the future [17, 18].

Traditional methods cannot easily capture data at high heights above buildings and over the ocean [19]. Despite the Hong Kong Observatory (HKO) aiming to follow World Meteorological Organization (WMO) guidelines by mounting automatic wind stations anemometers 10m above the ground [20, 21], WMO's guide states that this only applies to open areas where the distance between the anemometer and any obstacle is at least 10 times the height of the obstacle [2]. Instead, in WMO guidance on urban meteorological observations, Oke (2006) emphasized that collecting meaningful wind data in urban settings requires sensor mounting on a mount system higher than the widest dimension of the building's roof - an expensive and impractical approach [22]. Moreover, weather towers can only measure at fixed positions. Exacerbated by Hong Kong's diverse topography of hills, islands, and harbour, which causes large variations in wind, this sparse network of fixed stations is not enough to capture the city's complex wind environment [23].

On the other hand, UAVs (Unmanned Aerial Vehicles) offer a method to collect data with high spatial mobility, no building construction, lower cost and less maintenance requirements and space compared to traditional methods.

2.1 Proposed Solution

Hence, this study investigated the use of a Trisonica mini anemometer mounted vertically on top of a DJI Mavic 3E UAV, with a custom landing stand, to collect wind data in place of fixed, traditional sensors in Hong Kong. The study examined the relationship between boom length and propeller-induced disturbance detected by the anemometer, aiming to determine the optimal boom length between the anemometer and UAV body with minimal propeller-induced flow disturbance while maintaining flight stability and safety.

2.2 Outline of the Paper

Existing studies on the use of UAV to collect wind data are discussed in Section 3, along with their strengths, limitations, and current gaps in the field. Subsequently, the experiment methodology is discussed in Section 4, which describes the UAV's configuration, experiment set-up and procedure. Next, Section 6 compares the wind disturbance for each boom length. Interpretations of the results, relation of the results to other studies, and the significance of findings are discussed in Section 7. The limitations of the experiment, proposed design and suggestions for future work are discussed in Section 8.

3 Literature review

3.1 Types of UAVs

Three main types of UAVs exist: fixed-wing, single-rotor and multirotor. Fixed-wing and single-rotor UAVs usually require more space for takeoff and landing. In contrast, multirotor micro-UAVs - UAVs with maximum takeoff weight (MOTW) of 2kg - have emerged as a promising solution for wind measurements in dense urban environments [24, 25].The DJI Mavic 3E, with MOTW of 1.05 kg, falls into this category. Compared to larger UAVs, micro-UAVs are off-the-shelf, cheap, compact, portable, and can fly in tighly enclosed spaces. Their small sizes, maneuverability and vertical take-off/landing capabilities enable measurements close to buildings, in street canyons, and over complex terrain where traditional anemometers are few and other UAV types are operationally difficult to deploy [26, 27].

Unlike UAVs surpassing 7kg MOTW, according to Hong Kong's Small Unmanned Aircraft Order (Cap. 448G), the DJI Mavic 3E falls under category A2, allowing flight up to 300 ft from the ground without requiring prior approval from the Civil Aviation Department. Thus, although micro-UAVs have smaller available payload and battery life, they are advantageous for wind sensing in a high-rise, access-constrained city like Hong Kong [28].

3.2 Types of Wind Sensing Methods on UAVs

Multirotor UAV-based wind sensing strategies can be categorized into three types: direct, indirect and remote sensing.

Direct sensing mounts additional sensors, such as such as pressure probes, thermal anemometry and ultrasonic anemometers, on the drone to measure the wind directly. Pressure probes deduce wind from differential pressures but require careful calibration and are sensitive to angle of attack. Hence, for accurate sensing in multirotors, accurate measurements typically require attaching the probe outside of the rotor disk, complicating balance. Consequently, they are usually used for fixed-wing UAVs. Alternatively, thermal anemometers are more fragile and sensitive to changes in humidity, pollution, flying height and cleanliness of the anemometer, leading to lower usage. Due to high accuracy and data collection frequency, light weight, low power consumption, easy purchase and data analysis procedure, no moving parts and low maintenance, ultrasonic anemometers are the most commonly mounted sensors on UAVs, particularly the Triosonica and FT205 [1].

Indirect sensing does not attach another sensor to the vehicle, but analyzes how the UAV responds to the wind through onboard sensor data to mathematically calculate the features of the wind that caused it. The advantage is that, unlike direct sensing, the indirect sensing method avoids direct sensor immersion in rotor wash. For example, when Chen et al. used onboard data to develop a relationship between a UAV (with maximum takeoff mass of 9.0kg) tilt response and the wind, the indirect sensing method was more accurate than mounting a sonic anemometer at UAV climbing speeds above 2m/s. However, they found that due to the asymmetrical design of the UAV, changes in wind direction and payload configuration significantly affected the response of the UAV, hence requiring extensive training data and custom calibration for different UAV models to obtain accurate results [29]. Additionally, in low winds, the UAV exhibited dampened responses, increasing the measurement uncertainty. Overall, the indirect sensing method requires more pre-flight data collection, custom calibration and computational complexity.

In remote sensing using LiDAR, laser pulses are sent from the UAV, which bounce off particles in the air. Using the Doppler effect, the frequency change of the light echoing back to the vehicle is used to deduce the wind velocity. However, since such systems are heavy and have high power consumption, most existing applications rely on larger UAVs, or keep the LiDAR units on the ground [1, 30, 31]. Furthermore, LiDAR systems are more expensive compared to other methods.

Therefore, for wind sensing with the DJI Mavic 3E, mounting a Trisonica Mini anemometer offers the best balance of accuracy, cost, practicality and integration complexity.

3.3 Mounting geometry, rotor downwash, and operational integration

Propeller-induced flow or rotor wash is caused by UAV propellers creating a region of lower pressure above the drone, causing air to accelerate downward to generate thrust, resulting in a turbulent jet below the drone, and a suction zone above that distorts wind directly above the drone. Mounting the anemometer within these disturbance zones results in wind data not representative of the actual surrounding wind velocity.

While several studies propose sensor mounting distances proportional to rotor diameter (D), these guidelines remain specific to UAV geometries and fail to offer a scalable framework across varying multirotor configurations [34–38]. On the other hand, Pastay et al. established that sensor quiet-zone offsets scale directly with disk loading, requiring a vertical separation of $1.75R$ ($\approx$ 20.9 cm) at $DL = 100$ N/m^2, while recommending sensor placement at the system geometric center instead of axial locations about the individual rotors [39]. However, they only examined the quiet zones for multi-rotor disk loadings of 100 and 300 N/m2.

Three methods of mounting the anemometer are top, bottom and side mounting, with top mounting being the most common technique [1]. While side mounting allows the anemometer to sit outside the column of turbulent air, the asymmetric payload distribution results in stability issues, especially in

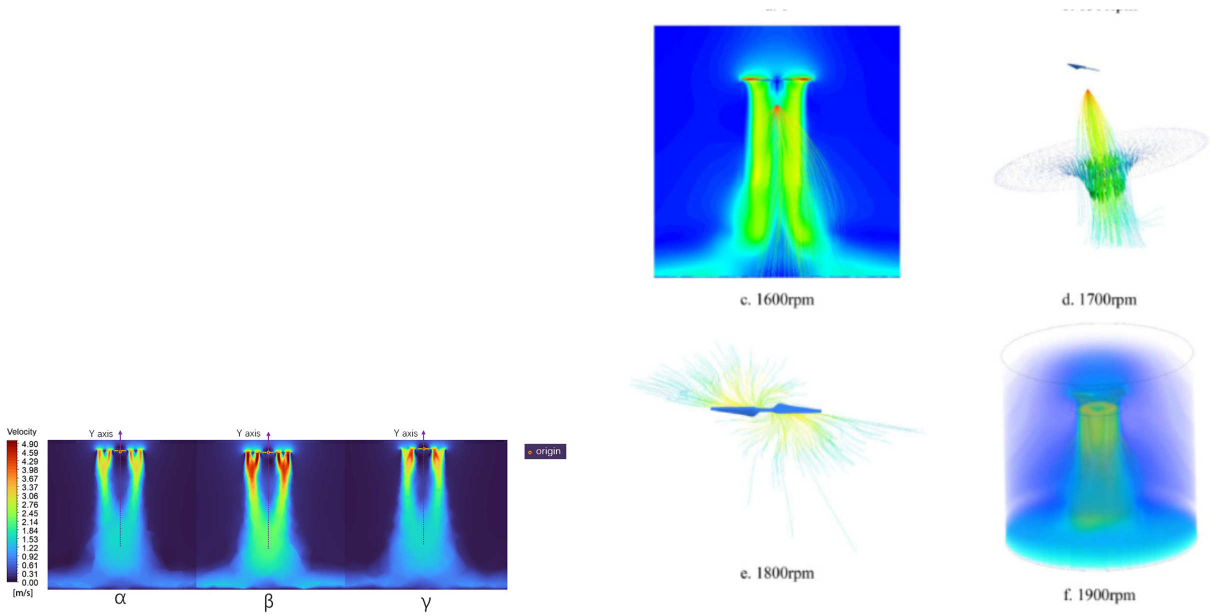

Figure 1: *CFD visualizations of UAV downwash and inflow characteristics by Liu et al. [32] and Chang et al. [33].*

smaller UAVs with tight center-of-gravity tolerances.

Although an bottom mount adds mass below the center of gravity and can increase the pendulum restoring moment, it also increases the moment of inertia and can reduce control performance, especially on small UAVs in gusty conditions. Even though there exists a small quiet zone directly below the drone body - supported by Liu et al. measuring 0.21 m/s minimum downwash velocity at 0.2m below the rotor plane [32] - bottom mounting also interferes with underbody obstacle detection sensors, especially for off-the-shelf UAVs. As can be seen from CFD visualization of airflow around a UAV by Chang et al. in Fig 1, the airflow above the rotor plane is also less turbulent than below [33].

Thus, the Trisonica Mini was mounted vertically above the UAV's geometric center for this study.

3.4 Gaps in Research in Micro-UAV direct wind sensing

Most existing use UAVs with MOTW above 2.5 kg, while research on micro-UAVs is limited [16, 34, 40, 41]. Existing studies typically employ top-mounted boom lengths of more than 30cm, as larger UAVs operate at higher thrust and disk loading to support heavier payloads, generating stronger downwash and a larger disturbed flow region. Given the lower disk loading of the micro-UAV used in this work, the study focused on shorter boom lengths in the 5–20cm range to assess whether acceptable accuracy can be achieved.

4 Methodology

4.1 UAV-Anemometer mount and Landing Stand Design

To integrate the TriSonica ultrasonic anemometer onto the DJI Mavic 3E aircraft, a custom mounting system was developed. The architecture was divided into top-mounted and underslung assemblies to optimize anemometer accuracy while maintaining mechanical stability:

- **Top-mounted Sensor:** The ultrasonic anemometer was positioned vertically above the drone's geometric center using a lightweight, PLA rod, shown in Fig 2. Elevating the sensor above the airframe distanced the anemometer from direct propeller-induced disturbance.

- **Underslung Hardware:** To offset the top-mounted mass and lower the aircraft's center of gravity (CG), support electronics - including a custom signal-conditioning Printed Circuit Board (PCB), battery power supply, and data-logging wires -were suspended beneath the airframe using lightweight zipties, shown in Fig 2.

- **Elevated Landing Stand:** Because the underslung hardware module extended below the drone arms, direct ground contact was unfeasible. A custom UAV stand was engineered to

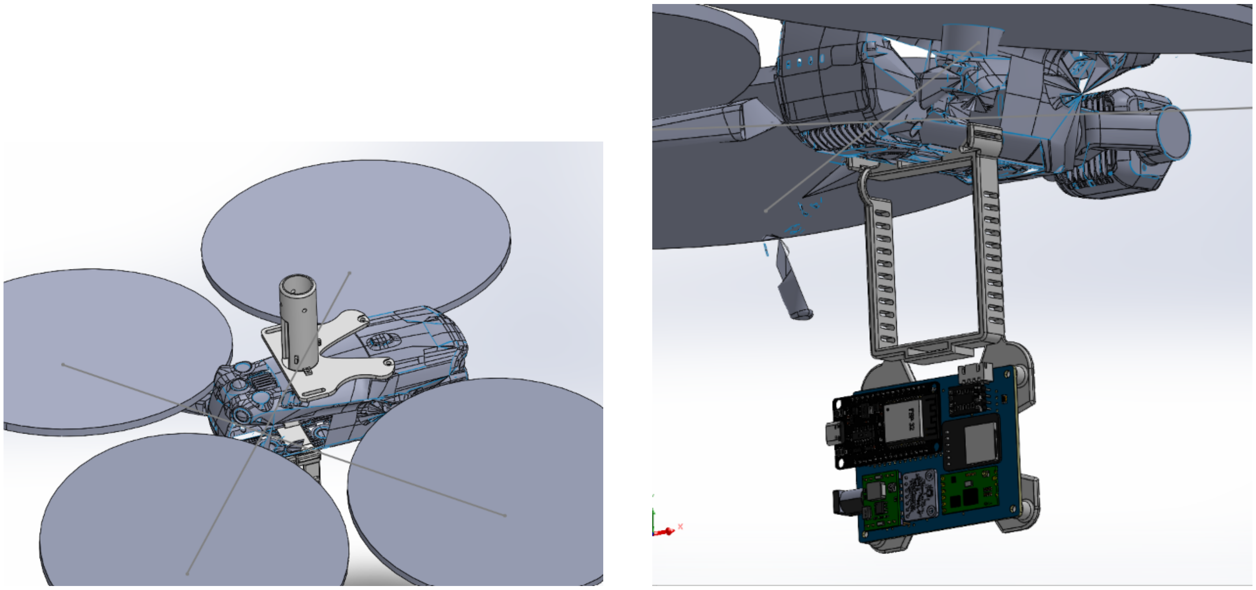

Figure 2: *CAD models of the drone setup showing the anemometer mounting (left) and the underslung battery pack and PCB secured via zip-ties (right).*

provide safe landing, protecting the underbody payload during takeoff and landing maneuvers, shown in Fig 3. The overall stand height was set to 1 m after prototype tests at lower elevations triggered the aircraft's downward obstacle avoidance sensors, which interpreted the stand structure as a ground hazard and preventing landing. Elevating the stand prevented false-positive proximity triggers and allowed successful landings. The landing interface itself was designed as a circular acrylic ring, providing 360° yaw alignment tolerance during descent and mitigating collision risks with the underslung module compared to earlier rectangular designs. Structurally, the frame was made of lightweight carbon fiber rods and a wooden base. The pyramidal design provided a low center of gravity for tip-over stability alongside mechanical compliance to absorb landing impact forces. All structural joints were additively manufactured using Polylactic Acid (PLA), incorporating C-clamp mechanisms and captive nut sockets. The result was a modular, highly portable stand that enabled rapid field assembly with minimal tools.

The final configuration is displayed in Fig 3 and weighed 1276.4 g without the carbon fiber rod, and 1304.1 g including the longest carbon rod (20cm).

4.2 Experimental Setup and Facility

A semi-outdoor measurement setup was deployed (as shown in Fig 4) with a target of flying the drone 3m from the ground. While testing indoors would allow downwash and airflow to bounce off surrounding obstacles, affecting sensor data, using a semi-open outdoor location reduced these recirculation effects, while protecting equipment from weather conditions.

To establish an accurate baseline for ambient wind speed, a 3m elevated aluminium mast, with the ultrasonic anemometer mounted at the top, was used to measure natural ambient wind velocity at the target flight altitude. To protect the PCB, the PCB was housed inside a plastic pouch and taped to the mass top, along with the battery pack. Three separate 2-minute ambient wind readings were collected at different times across different days. These trials were conducted at the exact same site under similar weather conditions, and the results were averaged to determine the baseline ambient wind speed prior to active drone testing.

4.3 Variable Isolation and Experiment Design

The independent variable in this experiment was the boom length (L). The primary dependent variables comprised the induced aerodynamic velocity disturbance (v_i), measurement RMSE relative to the baseline mast, flow tilt angle (θ), and turbulence intensity (σ). To ensure experimental consistency, controlled variables included: aircraft flight mode (GPS position-hold at a constant direction), hover altitude (2.0 m above the drone stand (3m from the ground), corresponding to $> 8D$ altitude to operate strictly

Figure 3: *CAD design of the drone stand (left) and the final physical assembly (right).*

Figure 4: *Experiment venue.*

Out-of-Ground-Effect), approximately constant system mass, axial sensor alignment along the central vehicle axis and data logging frequency.

To decide the boom length testing interval, the micro-UAV's disk loading($DL = W/A_{\text{total}}$) was calculated. For the DJI Mavic 3 Enterprise ($D = 0.2388$ m, total swept area $A_{\text{total}} = 0.1792$ m^2), the operational hover mass range (1.015–1.304 kg) yielded a low disk loading of $DL \approx 55.6$–71.4 N/m^2. Prior literature by Pastay et al. demonstrated the upper quiet zone above the drone was $\sim 1.75R$ ($\approx$ 20.9 cm) at $DL = 100$ N/m^2) above the rotor plane. Because our UAV operated well below this baseline, the theoretical disturbance dissipation threshold was predicted to fall at 20 cm ($1.68R$). Hence, an experimental interval of 5–20 cm ($0.42R$–$1.68R$) was selected, mapping the near-body flow gradient from the severe disturbance zone (5 cm) up to the theoretical decay boundary (20 cm).

4.4 Experimental Procedure

The anemometer was mounted onto the assembly with its North directional indicator aligned along the forward camera axis. Sensor wiring was secured clear of the propeller sweep plane with tape. Sensor logging was initialized by inserting a microSD card into the PCB logger, connecting the telemetry receiver to the ground station laptop, and supplying power to the PCB. Each data collection flight comprised a 2.0-minute ground-level ambient baseline logging period, followed by a vertical climb to a 3.0 m. After maintaining a steady-state hover for 2 minutes, the aircraft was landed. Following a 10-second interval, anemometer power source was disconnected, and the microSD card log file was transferred to the host computer and indexed by boom length.

5 Data Processing and Analysis Workflow

To process, clean, and evaluate the raw anemometer data collected across varying boom lengths, a custom data analysis program was developed in Python. Raw log files generated by the TriSonica sonic anemometer at 10 Hz were parsed using regular expression pattern matching to extract multi-axis wind components (U, V, W), scalar wind speed (S), and environmental metrics. The ingestion routine automatically filtered out initial sensor boot-up artifacts (e.g., -100) and unphysical outliers ($S \geq 30\,\mathrm{m/s}$).

To ensure the wind calculations only reflected stable hover conditions, the active analysis window was defined as starting when wind readings suddenly increased well above ambient baseline levels due to rotors turning on. Similarly, the window was stopped right before wind speeds dropped back down after descent and landing. This ensured Root Mean Square Error (RMSE), standard deviation, and turbulence intensity were calculated strictly from clean, steady-state hover data. Fig 5 shows an example of the manual analysis window selection for boom length of 20 cm.

During data processing, wind speed readings collected at a 14 cm boom length showed unusual and extreme fluctuations compared to other runs. When inspecting the raw wind speed trace, it was impossible to tell where the ground operations ended and where actual hovering began. Because the flight phases could not be clearly separated, the 14 cm dataset was identified as an anomaly and completely removed from the analysis to avoid skewing the overall results (Fig 5). Additionally, a test flight at boom length of 35 cm was performed, but no air data was collected due to the high instability of the aircraft.

For each tested boom length, the automated pipeline calculated key statistical turbulence and inflow metrics:

- **Induced Velocity (v_i):** Evaluated as:

$$v_i = S - V_{\mathrm{amb}} \tag{1}$$

- **Velocity Fluctuations & Quality:** Root-mean-square error (RMSE), standard deviation (σ_{v_i}), and threshold exceedance rate ($|v_i| > 1.0\,\mathrm{m/s}$).

- **Flow Deflection:** Inflow tilt angle derived from the vertical and scalar components:

$$\theta = \mathrm{atan2}(W, S) \tag{2}$$

- **Disturbance Ratio:** Normalized relative disturbance ratio (v_i/V_{amb}).

6 Results

6.1 Ambient Baseline Benchmark

The ambient wind velocity measured by the 3 m mast was $V_{amb} = 0.281$ m/s. All flow velocities above this value recorded during the experiments were due to additional velocity induced by propeller-induced disturbance.

6.2 Overall Disturbance Trends Across Boom Heights

As expected, propeller-induced disturbance generally decreased as the anemometer was raised further above the rotor plane. The 20 cm vertical boom achieved the best overall performance across most measured statistical metrics:

- **Lowest Measurement Error:** RMSE dropped to 0.853 m/s (compared to 1.287 m/s at 5 cm).
- **Lowest Induced Velocity:** Mean induced flow (v_i) reached a local minimum of 0.701 m/s.
- **Minimal Extreme Spikes:** High-speed error exceedance (> 1.0 m/s) fell to 25.64%, whereas closer positions exceeded 1.0 m/s over 50% of the time.
- **Lowest Disturbance Ratio:** The ratio of induced speed to ambient baseline (v_i/V_{amb}) reached its minimum at 2.631.

While the overall trend showed less disturbance at greater heights, the relationship between boom length and flow distortion was non-linear. At the 10 cm boom length, RMSE temporarily dropped to 0.957 m/s and mean induced velocity fell to 0.788 m/s. Exceedance above 1.0 m/s dropped sharply to 34.10% at 10 cm, compared to 56.31% at 7 cm and 52.70% at 11 cm. Notably, the flow detection angle closest to 0 was shown by the 10 cm boom length, even closer than the 20 cm boom length, indicating nearly horizontal incoming airflow and implying minimum vertical distortion. Conversely, flow detection angle deviated the most from 0 at boom length of 13 cm, implying maximum bending due to suction effect.

6.3 Flow Deflection and Turbulence Behavior

Negative tilt angles across all heights (ranging from -4.42° at 10 cm to -15.40° at 13 cm) confirmed that rotor suction continuously pulled incoming air

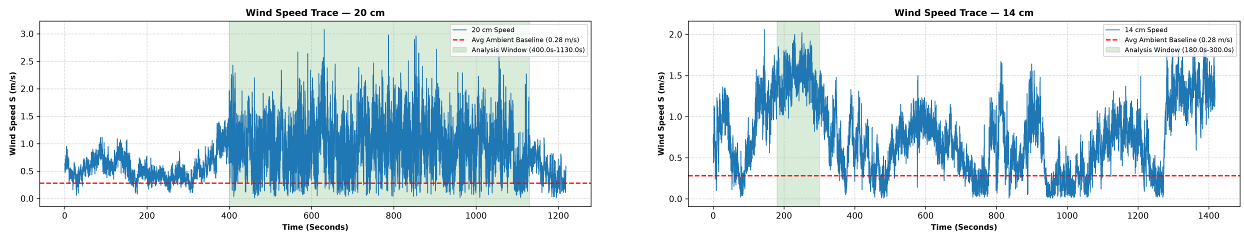

Figure 5: *Wind speed trace at the 20 cm constrained structural optimum showing the analysis window (left) compared to an anomalous raw wind trace at a lower boom height (right).*

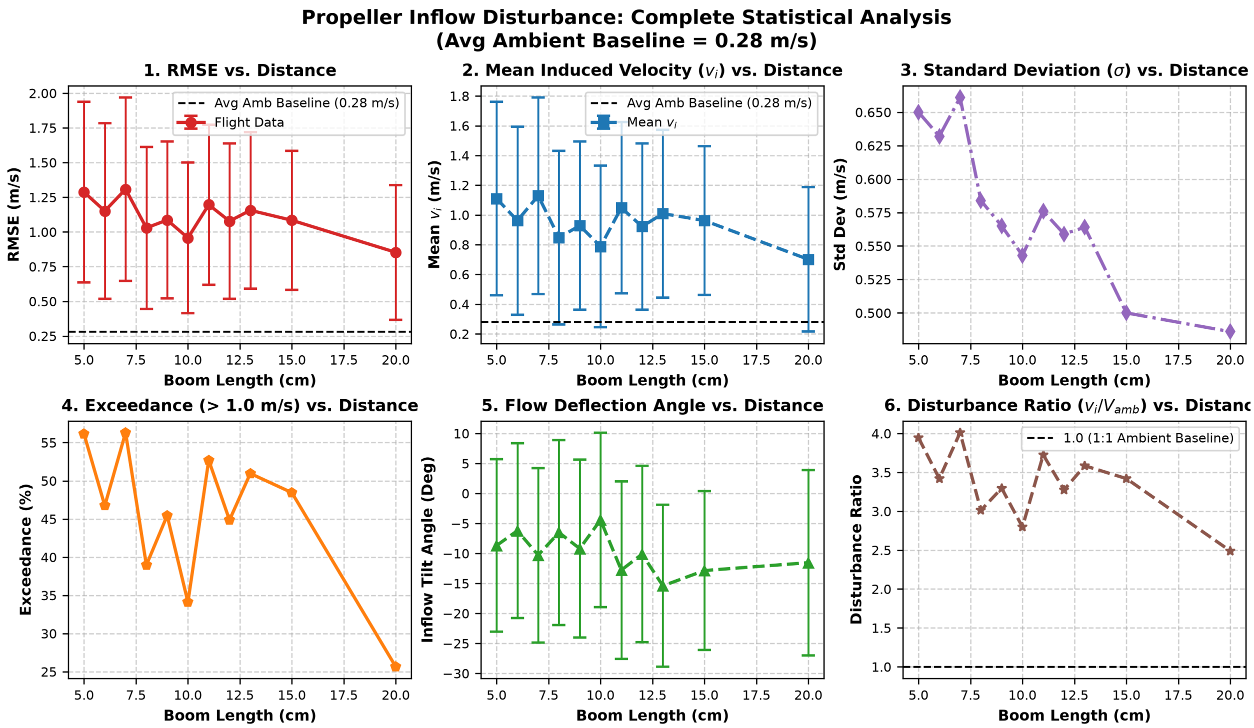

Figure 6: *Disturbance metrics across varying boom lengths, highlighting the 20 cm constrained structural optimum.*

downward toward the rotor plane. Standard deviation (σ) steadily declined from 0.650 m/s at 5 cm to 0.486 m/s at 20 cm, demonstrating that raising the sensor reduced high-frequency turbulent fluctuations alongside overall velocity errors.

7 Discussion

The overall decreasing trend of RMSE, mean induced velocity, standard deviation, exceedance and disturbance ratio confirmed the theoretical decay of propeller-induced inflow with distance from the rotor plane. The 20 cm length showed the least overall disturbance.

The results observed at 10 cm supported previous research that stated non-linear relationships between boom length and propeller-induced flow [42]. The effect was likely due to fuselage-induced displacement flow: near the top of the aircraft body, there existed a stagnation point where air velocity = 0 m/s. By Bernoulli's equation, the pressure at the stagnation point was maximum, creating a slight upward pressure gradient that partially canceled the downward pressure gradient created by the rotor suction. At a 10 cm elevation, these opposing vector components temporarily balanced, creating a small quiet zone before the suction effect re-dominated at 11-13 cm, before eventually decaying at 20 cm.

While the 20 cm configuration showed the highest measurement accuracy out of the boom lengths tested, the 10 cm boom achieved over 70% of the error reduction achieved at 20 cm while maintaining

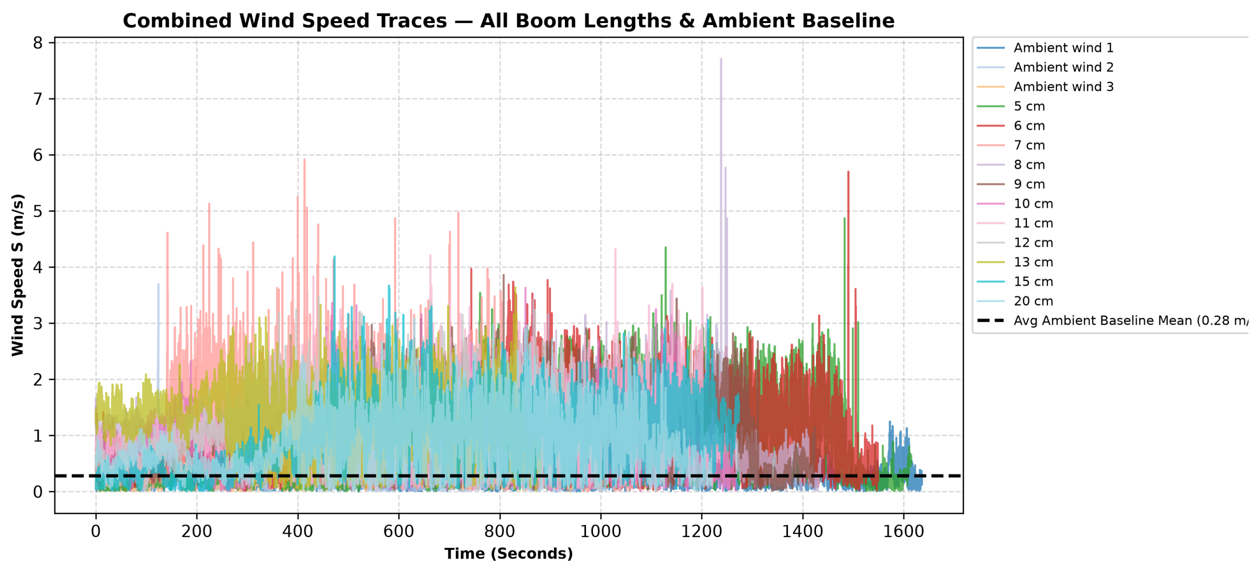

Figure 7: *Summary of raw wind traces across all tested configurations.*

Propeller Inflow Disturbance Summary

Composite Ambient Baseline (V_ambient): 0.281 m/s

Distance (cm)	RMSE (m/s)	Mean vi (m/s)	Std Dev (m/s)	Exceedance (%)	Tilt Angle (deg)	Tilt Std Dev (deg)	Disturbance Ratio
5	1.287	1.110	0.650	56.14	-8.68	14.39	3.945
6	1.151	0.962	0.632	46.74	-6.21	14.57	3.420
7	1.308	1.129	0.661	56.31	-10.29	14.54	4.011
8	1.029	0.848	0.584	38.96	-6.51	15.40	3.012
9	1.086	0.928	0.565	45.45	-9.19	14.81	3.296
10	0.957	0.788	0.543	34.10	-4.42	14.56	2.798
11	1.196	1.048	0.576	52.70	-12.78	14.78	3.725
12	1.078	0.922	0.559	44.86	-10.11	14.69	3.275
13	1.156	1.009	0.564	50.96	-15.40	13.50	3.585
15	1.084	0.962	0.500	48.45	-12.85	13.25	3.420
20	0.853	0.701	0.486	25.64	-11.54	15.46	2.490

Figure 8: *Statistical summary of experimental results illustrating error convergence.*

a more compact and stable configuration. Therefore, the 10 cm vertical boom is recommended as a compromise for micro-UAV wind-sensing in dense urban environments, whereas a 20 cm boom is recommended for stationary, higher accuracy data collection. On the other hand, the author advises against using a 13 cm boom length to avoid the high vertical distortion implied by its maximum tilt angle result.

8 Conclusion

This research confirms that the airflow interference caused by drone propellers generally decays as a wind sensor is moved higher above the rotors. For sheer measurement accuracy, the 20 cm vertical boom proved to be the most effective configuration, demonstrating the lowest overall velocity errors and minimal flow distortion. However, the relationship between height and air disturbance is not perfectly linear. A 10 cm boom length successfully leveraged a temporary balance in air pressure directly above the drone's body, creating a surprisingly clear "quiet zone" for the sensor. Ultimately, the 10 cm boom is recommended as the ideal compromise for agile wind-sensing in tight city environments, while the 20 cm configuration is best reserved for stationary, high-precision data collection.

9 Limitations

This study has several limitations that should be considered when interpreting the results.

First, boom lengths were evaluated only in the 5–20 cm range above the rotor plane. Longer extensions (e.g., 35 cm) were found in preliminary tests to induce unacceptable instability and safety risks on the DJI Mavic 3E, and were therefore not systematically tested. Thus, the identified optimal boom length represents the best length within this feasible design window, not necessarily a global optimum.

Second, all experiments were conducted on a single UAV platform (DJI Mavic 3E) with a fixed payload (TriSonica Mini anemometer and custom mount). Results may not generalize directly to other micro-UAVs with different mass, rotor size, disk loading, or flight control characteristics.

Third, flights were conducted under a limited range of environmental conditions and primarily in hover. The influence of stronger winds, gusty conditions, and other flight modes (climb, descent, horizontal translation) on the optimal boom length was not fully explored.

Fourth, the drone's wind sensor and the ground reference station could not be placed at the exact same spot or height for every flight. Although we tried to maintain the approximate flight position, this slight separation means some of the errors in the data may be due to natural wind differences across space, rather than propeller interference. Additionally, we did not perform any wind-tunnel testing or specialized field calibrations for this specific drone setup. While the results are significant for comparing how different boom lengths perform against one another, these factors mean the absolute measurements may have a small margin of error.

Finally, the number of flights and total sampling duration were limited by project timeline and weather constraints. While the observed trends were consistent across multiple flights, a larger dataset would improve statistical confidence.

Despite these limitations, the present study provides a practical, empirically based design guideline for mounting ultrasonic anemometers on micro-UAVs in urban environments. Future work should explore longer boom lengths, conduct systematic calibration against reference towers, and evaluate performance under a wider range of atmospheric conditions and flight profiles.

References

[1] Mohammadamin Soltaninezhad, Roberto Monsorno, and Stefano Tondini. A review of methods and challenges for wind measurement by small unmanned aerial vehicles. Meteorol. Appl., 32(3), May 2025.

[2] https://www.weather.gov/media/epz/mesonet/CWOP-WMO8.pdf. [Accessed 05-09-2026].

[3] Researching the risks — croucher.org.hk. https://croucher.org.hk/en/news/researching-the-risks. [Accessed 28-08-2026].

[4] Hong Kong Observatory. Typhoon 5-6 (average number of tropical cyclones). https://www.hko.gov.hk/en/education/tropical-cyclone/classification-naming-characteristics/00161-typhoon-56-average-number-of-tropical-cyclones.html. [Accessed 28-08-2026].

[5] Tropical Cyclones in 2018 ¿ Report on Super Typhoon Mangkhut (1822): 7 – 17 September 2018 — hko.gov.hk. https://www.hko.gov.hk/en/publica/tc/tc2018/section3_5rpt.html. [Accessed 28-08-2026].

[6] Tropical Cyclones in 2018 ¿ Annex 1: Estimated Direct Economic Losses in Hong Kong caused by Super Typhoon Mangkhut (1822) — hko.gov.hk. https://www.hko.gov.hk/en/publica/tc/tc2018/annex1.html. [Accessed 28-08-2026].

[7] Edward NG. Wind and heat environment in densely built urban areas in hong kong. Global Environmental Research, 13(2):169–178, 2009.

[8] Top-notch experts to assess impact of Urban Heat Island effects - PolyU — polyu.edu.hk. https://www.polyu.edu.hk/archive/media-releases/en/index_id_1640.html. [Accessed 28-08-2026].

[9] Statement on Climate Change (February 2023) – HONG KONG METEOROLOGICAL SOCIETY — meteorology.org.hk. https://www.meteorology.org.hk/new/statement-on-climate-change/. [Accessed 28-08-2026].

[10] Ronghui Qi, Lin Lu, and Hongxing Yang. Impact of climate change on ventilation load and energy use of air conditioning systems in buildings of hong kong. International Journal of Low-Carbon Technologies, 7(4):303–309, 12 2012.

[11] Transport Department - Introduction — td.gov.hk. https://www.td.gov.hk/en/transport_in_hong_kong/its/introduction/index.html. [Accessed 28-08-2026].

[12] Table HM-10 - Highway Statistics 2022 - Policy — Federal Highway Administration — fhwa.dot.gov. https://www.fhwa.dot.gov/policyinformation/statistics/2022/hm10.cfm. [Accessed 28-08-2026].

[13] Table MV-1 - Highway Statistics 2022 - Policy — Federal Highway Administration — fhwa.dot.gov. https://www.fhwa.dot.gov/policyinformation/statistics/2022/mv1.cfm. [Accessed 28-08-2026].

[14] Edward Ng. Policies and technical guidelines for urban planning of high-density cities - air ventilation assessment (AVA) of hong kong. Build. Environ., 44(7):1478–1488, July 2009.

[15] 2024 Annual Air Quality Review - Clean Air Network — hongkongcan.org. https://hongkongcan.org/press-release/annual-air-quality-review-2024-pollution-reduced-but-still-incurred-high-health-and-economic-costs/. [Accessed 28-08-2026].

[16] Ross T. Palomaki, Nathan T. Rose, Michael van den Bossche, Thomas J. Sherman, and Stephan F. J. De Wekker. Wind estimation in the lower atmosphere using multirotor aircraft. Journal of Atmospheric and Oceanic Technology, 34(5):1183 – 1191, 2017.

[17] https://www.pland.gov.hk/file/planning_studies/comp_s/hk2030plus/document/Land%20Supply%20Considerations%20and%20Approach_Eng.pdf. [Accessed 01-09-2026].

[18] https://www.legco.gov.hk/yr17-18/english/panels/dev/papers/dev20180529-pamphlet201804-e.pdf. [Accessed 01-09-2026].

[19] Z.R. Shu, Q.S. Li, Y.C. He, and P.W. Chan. Observations of offshore wind characteristics by doppler-lidar for wind energy applications. Applied Energy, 169:150–163, 2016.

[20] Surface Meteorological Measurements in Hong Kong — hko.gov.hk. https://www.hko.gov.hk/en/wservice/tsheet/sfmet.htm. [Accessed 05-09-2026].

[21] Lite but Loaded – Co-WIN Automatic Weather Stations — hko.gov.hk. https://www.hko.gov.hk/en/Observatorys-Blog/106239/Lite-but-Loaded-%E2%80%93-Co-WIN-Automatic-Weather-Stations. [Accessed 05-09-2026].

[22] urban-climate.org. https://urban-climate.org/wp-content/uploads/2023/10/Oke_2006_IOM-81-UrbanMetObs.pdf. [Accessed 01-09-2026].

[23] Steve Hung Lam Yim. Development of a 3D real-time atmospheric monitoring system (3DREAMS) using doppler LiDARs and applications for long-term analysis and hot-and-polluted episodes. Remote Sens. (Basel), 12(6):1036, March 2020.

[24] Nano-UAV and micro-UAV developments — euro-sd.com. https://euro-sd.com/2024/04/articles/37409/nano-uav-and-micro-uav-developments/. [Accessed 10-09-2026].

[25] NCAS. Hover to measure: Meet the drones of atmospheric science. https://ncas.ac.uk/hover-to-measure-meet-the-drones-of-atmospheric-science/. [Accessed 10-09-2026].

[26] Expansion of open-source drone software to include wind analysis - eprints — eprints.ost.ch. https://eprints.ost.ch/id/eprint/1356/. [Accessed 10-09-2026].

[27] Johannes Kistner, Julian Jüchter, and Norman Wildmann. High-resolution vertical wind and turbulence measurements with quadcopter uncrewed aerial systems: wind tunnel calibration and field validation, 2026.

[28] Civil Aviation Department - Small Unmanned Aircraft Order (Cap.448G) — cad.gov.hk. https://www.cad.gov.hk/english/sua_overview_categorisation.html. [Accessed 14-09-2026].

[29] D. Chen, W. Su, S. Jiang, H. Yang, C. Zhang, S. Jiang, D. Chang, Y. Liang, H. Wang, X. Yang, T.-M. Fu, Z. Zeng, L. Zhu, H. Shen, C. Wang, and J. Ye. Wind estimation based on flight dynamics of unmanned aerial vehicle: influencing variables and its environmental application. Atmospheric Chemistry and Physics, 26(5):3607–3620, 2026.

[30] A. R. Segales, T. M. Bell, A. A. Tasim, A. Quiroz, J. D. Simms, J. G. Gebauer, and E. N. Smith. Coptersonde-swx: development of a uas-based vertical atmospheric profiler for severe weather. Atmospheric Measurement Techniques, 19(11):3667–3686, 2026.

[31] Xu Zhang, Zhifeng Lin, Ran Wang, Siyuan Hu, Yiyang Zheng, Di Mo, and Changjun Ke. Miniaturized coherent doppler wind lidar with self-compensating harris hawks optimization algorithm for low-altitude uav-borne wind sensing. Remote Sensing, 18(11), 2026.

[32] Zongru Liu, Rong Gao, Yinwei Zhao, Han Wu, Yunting Liang, Ke Liang, Dong Liu, Taoran Huang, Shaoqiang Xie, Jia Lv, and Jiyu Li. Study on the characteristics of downwash field range and consistency of spray deposition of agricultural uavs. Agriculture, 14:931, 06 2024.

[33] Kun Chang, Shengde Chen, Meimei Wang, Junwei Liu, Ziming Zeng, and Yubin Lan. Simulation and verification of coupling characteristics of downwash airflow field and droplet field of agricultural unmanned aerial vehicle. Smart Agricultural Technology, 13:101737, 2026.

[34] W. Thielicke, W. Hübert, U. Müller, M. Eggert, and P. Wilhelm. Towards accurate and practical drone-based wind measurements with an ultrasonic anemometer. Atmospheric Measurement Techniques, 14(2):1303–1318, 2021.

[35] Trevor C. Wilson, James Brenner, Zachary Morrison, Jamey D. Jacob, and Brian R. Elbing. Wind speed statistics from a small uas and its sensitivity to sensor location. Atmosphere, 13(3), 2022.

[36] Mauro Ghirardelli, Stephan T. Kral, Nicolas Carlo Müller, Richard Hann, Etienne Cheynet, and Joachim Reuder. Flow structure around a multicopter drone: A computational fluid dynamics analysis for sensor placement considerations. Drones, 7(7), 2023.

[37] M. Ghirardelli, S. T. Kral, E. Cheynet, and J. Reuder. Samurai-s: Sonic anemometer on a multi-rotor drone for atmospheric turbulence investigation in a sling load configuration. Atmospheric Measurement Techniques, 18(9):2103–2124, 2025.

[38] L. Jin, M. Ghirardelli, J. Mann, M. Sjöholm, S. T. Kral, and J. Reuder. Rotary-wing drone-induced flow – comparison of simulations with lidar measurements. Atmospheric Measurement Techniques, 17(9):2721–2737, 2024.

[39] Ashish Pastay, Shrivathsan Narayanan, and Bharath Govindarajan. Aerodynamic evaluation of wind speed sensor placement on UAVs for meteorological applications. March 2026.

[40] C. Ingenhorst, G. Jacobs, L. Stößel, R. Schelenz, and B. Juretzki. Method for airborne measurement of the spatial wind speed distribution above complex terrain. Wind Energy Science, 6(2):427–440, 2021.

[41] Kevin Adkins, Christopher Swinford, Peter Wambolt, and Gordon Bease. Development of a sensor suite for atmospheric boundary layer measurement with a small multirotor unmanned aerial system. International Journal of Aviation, Aeronautics, and Aerospace, 01 2020.

[42] Christian Eckert, Feifei Tong, Daniel P. Harrison, and Brendan P. Kelaher. Quantifying drone propeller-induced flow for optimal aerosol sensor placement. Physics of Fluids, 38(1):015179, 01 2026.